



Frasson, R. P. D. M., Pavelsky, T. M., Fonstad, M. A., Durand, M. T., Allen, G. H., Schumann, G., Lion, C., Beighley, R. E., & Yang, X. (2019). Global Relationships Between River Width, Slope, Catchment Area, Meander Wavelength, Sinuosity, and Discharge. *Geophysical Research Letters*, 46(6), 3252-3262.
<https://doi.org/10.1029/2019GL082027>

Publisher's PDF, also known as Version of record

License (if available):
Other

Link to published version (if available):
[10.1029/2019GL082027](https://doi.org/10.1029/2019GL082027)

[Link to publication record in Explore Bristol Research](#)
PDF-document

This is the final published version of the article (version of record). It first appeared online via Wiley at <https://doi.org/10.1029/2019GL082027> . Please refer to any applicable terms of use of the publisher.

University of Bristol - Explore Bristol Research

General rights

This document is made available in accordance with publisher policies. Please cite only the published version using the reference above. Full terms of use are available:
<http://www.bristol.ac.uk/red/research-policy/pure/user-guides/ebr-terms/>

Geophysical Research Letters

RESEARCH LETTER

10.1029/2019GL082027

Key Points:

- Using satellite imagery, meander wavelength and sinuosity were computed globally for the first time
- Even when extended to global scales, classical relationships between river width and meander wavelength and discharge still hold
- We found strong associations between sinuosity, width, meander wavelength, slope, and discharge

Supporting Information:

- Supporting Information S1

Correspondence to:

R. P. de Moraes Frasson,
frasson.1@osu.edu

Citation:

Frasson, R. P. d. M., Pavelsky, T. M., Fonstad, M. A., Durand, M. T., Allen, G. H., Schumann, G., et al. (2019). Global relationships between river width, slope, catchment area, meander wavelength, sinuosity, and discharge. *Geophysical Research Letters*, *46*, 3252–3262. <https://doi.org/10.1029/2019GL082027>








Received 11 JAN 2019

Accepted 8 MAR 2019

Accepted article online 15 MAR 2019

Published online 25 MAR 2019

Global Relationships Between River Width, Slope, Catchment Area, Meander Wavelength, Sinuosity, and Discharge

Renato Prata de Moraes Frasson¹ , Tamlin M. Pavelsky² , Mark A. Fonstad³ , Michael T. Durand^{1,4} , George H. Allen⁵ , Guy Schumann^{6,7} , Christine Lion⁸, R. Edward Beighley⁹, and Xiao Yang² 

¹Byrd Polar and Climate Research Center, The Ohio State University, Columbus, OH, USA, ²Department of Geological Sciences, University of North Carolina, Chapel Hill, NC, USA, ³Department of Geography, University of Oregon, Eugene, OR, USA, ⁴School of Earth Sciences, The Ohio State University, Columbus, OH, USA, ⁵Department of Geography, Texas A&M University, College Station, TX, USA, ⁶Remote Sensing Solutions, Inc., Monrovia, CA, USA, ⁷School of Geographical Sciences, University of Bristol, Bristol, UK, ⁸FluroSat Pty, Ltd, Eveleigh NSW, Australia, ⁹Department of Civil and Environmental Engineering, Northeastern University, Boston, MA, USA

Abstract Using river centerlines created with Landsat images and the Shuttle Radar Topography Mission digital elevation model, we created spatially continuous maps of mean annual flow river width, slope, meander wavelength, sinuosity, and catchment area for all rivers wider than 90 m located between 60°N and 56°S. We analyzed the distributions of these properties, identified their typical ranges, and explored relationships between river planform and slope. We found width to be directly associated with the magnitude of meander wavelength and catchment area. Moreover, we found that narrower rivers show a larger range of slope and sinuosity values than wider rivers. Finally, by comparing simulated discharge from a water balance model with measured widths, we show that power laws between mean annual discharge and width can predict width typically to −35% to +81%, even when a single relationship is applied across all rivers with discharge ranging from 100 to 50,000 m³/s.

Plain Language Summary For years, scientists and engineers have been using aerial photography to study the shapes of rivers, how they change over time, and how they relate to other river characteristics, such as river width, the slope of the water surface, and flow. These studies served as basis for the development of theories describing erosion, sediment transport, the speed at which flood waves travel through a basin, and serving as guidance for the measurement of river flow. However, such studies were often conducted in person, or done by combining results from other authors, leading to a very limited coverage of world rivers, most of which were in North America. As images of world rivers obtained by satellites became available and adequate computational power became affordable, we were able to describe the shape of worldwide rivers and how other properties, such as slope, width, and flow relate to meander characteristics. We showed that although classical geomorphic studies had limited geographical coverage, their results could generally be applied to typical rivers over the world. Additionally, with our results, rivers with atypical meander characteristics can be better identified, allowing the advancement of our understanding of how rivers work.

1. Introduction

Responding to the need for better understanding of rivers at continental and global scales, recent studies have explored existing remote sensing data to trace river networks (e.g., Allen & Pavelsky, 2015; Lehner et al., 2008; Lehner & Grill, 2013; Yamazaki et al., 2014), extract basin and floodplain parameters and features (Nardi et al., 2019; Shen et al., 2017), map the extent of flooding and flood risk (Andreadis et al., 2017; Brakenridge, 2018; Van Dijk et al., 2016), and estimate discharge (e.g., Brakenridge et al., 2007; Gleason et al., 2014; Gleason & Smith, 2014; Gleason & Wang, 2015; Tarpanelli et al., 2013; Tourian et al., 2013; Tourian et al., 2017). However, additional information about rivers can be extracted from currently available satellite imagery, particularly descriptors of shapes of rivers and meanders.

The use of aerial imagery for measuring river morphological traits such as meander wavelength and sinuosity has long been common practice in fluvial geomorphology (Allen et al., 2013; Constantine et al., 2014;

Marcus & Fonstad, 2008). Using measurements collected through either topographic surveys or aerial photographs, relationships between planform properties such as width and meander wavelength (e.g., Leopold & Wolman, 1960; Richards, 1982; Williams, 1986) have been identified. These relationships supported the development of theories regarding the dynamics of river meanders (e.g., Edwards & Smith, 2002; Seminara, 2006), and they continue to guide the definition of spatial scales over which to evaluate flow resistance (Bjerklie, 2007; Bjerklie et al., 2005) and to compute sinuosity (e.g., Kiel, 2015). Nevertheless, such relationships are usually derived based on data with limited geographical coverage. For example, Leopold and Wolman (1960) examined 49 rivers in the United States and Williams (1986) worked with 194 reaches, most of which are located in the United States and Canada, though a few sites are in India, Pakistan, Sweden, and Australia. This rather limited geographical coverage may impact the applicability of such relationships in underrepresented regions of the world.

Automated centerline tracing tools such as RivWidth (Pavelsky & Smith, 2008) allow the extraction of river centerlines from satellite imagery, from which one can identify river meanders and compute meander wavelength and sinuosity. Given the quasi worldwide coverage and recently improved ease of access to such images, we can now explore how these classical relationships hold when applied to rivers distributed over the globe. Moreover, by cross-referencing river extents obtained by Allen and Pavelsky (2018) with elevations measured by the Shuttle Radar Topography Mission (SRTM), water surface slopes can be estimated (LeFavour & Alsdorf, 2005), allowing, for the first time, an examination of global relationships between slope and river width and the evaluation of classical relationships between river width and meander wavelength at the global scale.

This work takes advantage of the river centerlines contained in the Global River Width from Landsat database (Allen & Pavelsky, 2015, 2018), which is briefly described in section 2.1, to compute meander wavelength and river sinuosity (section 2.2). Subsequently, we extracted water surface elevations from the digital elevation model obtained from the SRTM and computed water surface slopes after LeFavour and Alsdorf (2005) and mapped HydroSHEDS (Lehner et al., 2008; Lehner & Grill, 2013) catchment areas into our river centerlines as detailed in section 2.3. The resulting multivariable data set allowed quasi-global comparisons between river width, meander wavelength, sinuosity, water surface slopes, and mean annual flow obtained from the water balance model WBMsed (Cohen et al., 2014; section 3). Our analysis aims to evaluate how well previously established relationships between river properties hold when extended to global scales and to generate a range of hypotheses suitable for future studies that may benefit from our novel data set.

2. Data and Methods

2.1. River Centerlines and Widths

The methodology for the extraction of river centerlines and estimation of river widths is described in detail by Allen and Pavelsky (2015), and more recently by Allen and Pavelsky (2018). The major steps in the tracing of river centerlines and calculation of widths are the identification of the time of the year most likely to correspond to mean annual flow, which is executed using monthly discharges from the Global Runoff Data Center (GRDC, 2011); selection of the closest ice- and cloud-free Landsat scenes to the identified date; creation of a land-water mask based on dynamic thresholding (Li & Sheng, 2012) applied to the modified normalized difference water index calculated from Landsat reflectance values (Xu, 2006); and finally processing of the masks by employing the RivWidth software (Pavelsky & Smith, 2008) to trace centerlines and calculate river widths. This method allows the tracing of centerlines of rivers as narrow as 30 m, however, as widths of rivers narrower than 90 m tend to be overestimated (Allen & Pavelsky, 2015), streams narrower than 90 m were kept in our data set but excluded from our statistical analyses.

2.2. Meander Wavelength and Sinuosity

We calculated the meander wavelength as twice the distance between successive inflection points identified over river centerlines, as defined by Leopold and Wolman (1957). The inflection point identification followed a modified version of the method proposed by Bjerklie (2007): we operated one river segment at a time, defined here as a continuous section of a river centerline broken at the location of confluences. We projected the entire segment centerline using the Universal Transverse Mercator zone containing the

centroid of the segment. Next, we smoothed the projected centerline using a 5-point moving average to remove jagged edges caused by the finite raster resolution of the Landsat images. Finally, moving along the river segment, we identified the direction of the curvature of the river by the sign of the cross-product between two vectors: one beginning at the immediate upstream point and ending at the evaluated point and the second beginning at that point and ending at the immediate downstream point. Locations where the cross-product changed signs marked the locations where curvatures changed directions, therefore delimiting the meanders. We computed sinuosity over all identified meanders, regardless of whether the channel formed a symmetric S shape. We used the meander endpoints to delimit the length over which sinuosity is calculated according to its classic definition given in Leopold and Wolman (1960), that is, the ratio between the length measured along the centerline to half the meander wavelength.

2.3. River Slope and Catchment Area

Catchment area was derived from flow direction and corresponding flow accumulation grids based on HydroSHEDS (Lehner et al., 2008), which provides river networks obtained from SRTM data analysis and includes corrections based on observed hydrographic data sets. The flow accumulation grid describes, for any location (i.e., pixel), the number of upstream pixels that drain to that location. HydroSHEDS pixels were mapped into our centerlines using the nearest neighbor method. We translated flow accumulation given in number of pixels into catchment area (in m^2) by multiplying the number of pixels flowing to a location by the average area covered by 3 arc-seconds SRTM pixels according to the latitude of the centroid of the river segment. We show a limited evaluation of the catchment areas over the Mississippi River in the section 5 of the supporting information.

We matched SRTM pixels to river centerline points based on the nearest neighbor method. The matching allowed the use of flow distance computed from the Global River Width from Landsat centerlines, which accounts for river meanders not captured by HydroSHEDS, thus leading to better slope estimates than computing slopes from SRTM/HydroSHEDS alone. We attenuated SRTM elevation noise by applying a Gaussian filter over 10 km reaches, which were used to compute an initial estimate of the water surface slope using either least squares linear regression or the Theil-Sen estimator (Sen, 1968; Theil, 1992), a nonparametric method for robust fitting of first degree polynomials. We selected the slope given with the highest coefficient of determination as the initial estimate of the water surface slope. Next, we used the initial slope estimates to identify optimal reach lengths (RL) according to LeFavour and Alsdorf (2005), who showed that for calculating a reliable slope from SRTM, RL need to extend sufficient distances to accommodate the height errors (σ), given the minimum slope to be resolved (S_{\min}):

$$2 \sigma / \text{RL} = S_{\min}. \quad (1)$$

Using the initial slope estimates computed over 10 km reaches and assuming a constant SRTM error of ± 5.51 m (LeFavour & Alsdorf, 2005), we estimated new RL with equation (1) for each river segment. Finally, we recalculated water surface slopes over optimized RL. We omitted river reaches with slopes in excess of 300 cm/km, which generally occur in mountainous areas where SRTM is known to be inaccurate (Farr et al., 2007). As the SRTM data coverage is restricted to latitudes between 60°N and 56°S, the resulting data set is also restricted to 60°N and 56°S.

2.4. Relating River Width With Catchment Area

We assumed that the relationship between river width and catchment area follows a power law of the form

$$W = a \cdot A^b, \quad (2)$$

where W stands for the river width, A for the catchment area, and coefficients a and b are fitted using reduced major axis regression (Mark et al., 1977) applied in logarithm space. Reduced major axis was chosen over ordinary least-squares regression because it is robust to situations where the both variables, here width and catchment area, are measured with significant error. Calibration was performed using the `mcr` R package (Manuilova et al., 2014) using Deming regression on log-transformed widths and catchment areas. In order to reduce redundancy, the calibration data included only a single width-catchment area pair for each river segment.

3. Results and Discussion

We created a data set of quasi-global coverage, which allows the visualization of the evolution and the inter-connection of river planform properties and flow profile characteristics. As an example, Figure 1 shows the width, slope, meander wavelength, and sinuosity computed for the main stem of the Amazon River and tributaries. A closer inspection of Figure 1a depicts river widths gradually increasing as the Amazon tributaries flow from the Andes to the Atlantic Ocean, with abrupt width increases occurring at confluences. Similarly, Figure 1b shows the transition from steeper to mild slopes as tributaries merge and flow to the ocean. Contrasting Figures 1a and 1b, one can see that steeper slopes, for example, steeper than 70 cm/km, are more frequent in narrower streams, with widths less than or equal to 100 m and, generally, as rivers become wider, they tend to show shallower slopes. Figures 1c and 1d show the meander wavelength and sinuosity of channels, respectively, which, when compared to widths, illustrate the increasing wavelength and decreasing sinuosity as width increases. The increase of meander wavelength with width is expected as several authors have reported positive correlations between wavelength and width (e.g., Leopold & Wolman, 1960; Richards, 1976, 1982; Williams, 1986), however, we observed frequent deviations from previously reported linear relationships, which can be quantified by analyzing the histogram of the ratio between meander wavelength and width (Figure 2e).

We summarized the distributions and quantiles of river width, sinuosity, meander wavelength, water surface slope, ratio between the meander wavelength and width, and catchment area in Figures 2a–2f, respectively. The presented histograms and quantiles of river properties account for channels that are at least 90 m wide and with sinuosity greater than 1.01 at the 30 m point scale, that is, the number of occurrences per class multiplied by 30 m can be interpreted as river length per property class. Right skewness is common to all histograms in Figure 2, with higher skewness being associated with width, sinuosity, and catchment area.

The ratio between meander wavelength and channel width has been reported by many classical studies, for example, approximately 11 by Leopold and Wolman (1960), 12.34 by Richards (1976) and Richards (1982), and 7.5 by Williams (1986). Contrasting previous measurements with our findings, we see that the value reported by Leopold and Wolman (1960) was located between the mode of the distribution, 9, and the median, 12.67, whereas Richards (1976) was remarkably close to the worldwide median. However, the spread of the meander wavelength to channel width ratio (Figure 3b) indicates that significant errors may occur when using width to predict meander wavelength of a river. Analyzing the spatial variability of this ratio and cross-referencing it with other properties such as soil type databases, for example, the 1° grid Global Soil Types (Zobler, 1999), may shed some light on the reasons for the observed variability and possibly lead to an increased understanding of the factors governing the geometry of meanders.

Although not immediately comparable to our sinuosity results, both Leopold and Wolman (1960) and Richards (1976) also suggest that sinuosity is not normally distributed. An inspection of the histogram of sinuosity over the 49 rivers reported by Leopold and Wolman (1960) shows strong right skewness similar to that of Figure 2b. Nevertheless, sinuosity in both past studies is considerably larger than what we found, with Leopold and Wolman (1960) showing an average sinuosity value of 1.53 and Richards (1976) reporting an average between 1.25 and 1.38 depending on how reaches are defined for the computation of sinuosity. Aside from the vastly different sample size in our study, another difference arises: Leopold and Wolman (1960) only compute sinuosity at locations where meanders assumed a reasonably symmetrical S shape, whereas we did not enforce any symmetry.

Figure 3 depicts how width, slope, meander wavelength, and sinuosity are interconnected. Figure 3a indicates that, generally, water surface slope decreases as width increases. Figure 3b illustrates the coupling between meander wavelength and width. Figures 3c and 3d show that as slope and width increase, the range of possible sinuosity values decreases. Finally, Figure 3e relates river width and catchment area.

To assess the constancy of the meander wavelength to width ratio across different river widths, we split the rivers into four subsets: narrower than 100 m, wider than 100 m and narrower than 200 m, $200\text{ m} \leq \text{width} < 300\text{ m}$, and wider than 300 m. We observed that as width increased, the mean meander wavelength to width ratio decreased, showing values of 21.2, 17.7, 13.2, and 8.4 for the four subsets, respectively, indicating a slowing down in the increase of the meander wavelength with width and offering another reason for the discrepancy between our results and those of past studies. Future analysis of our data set could

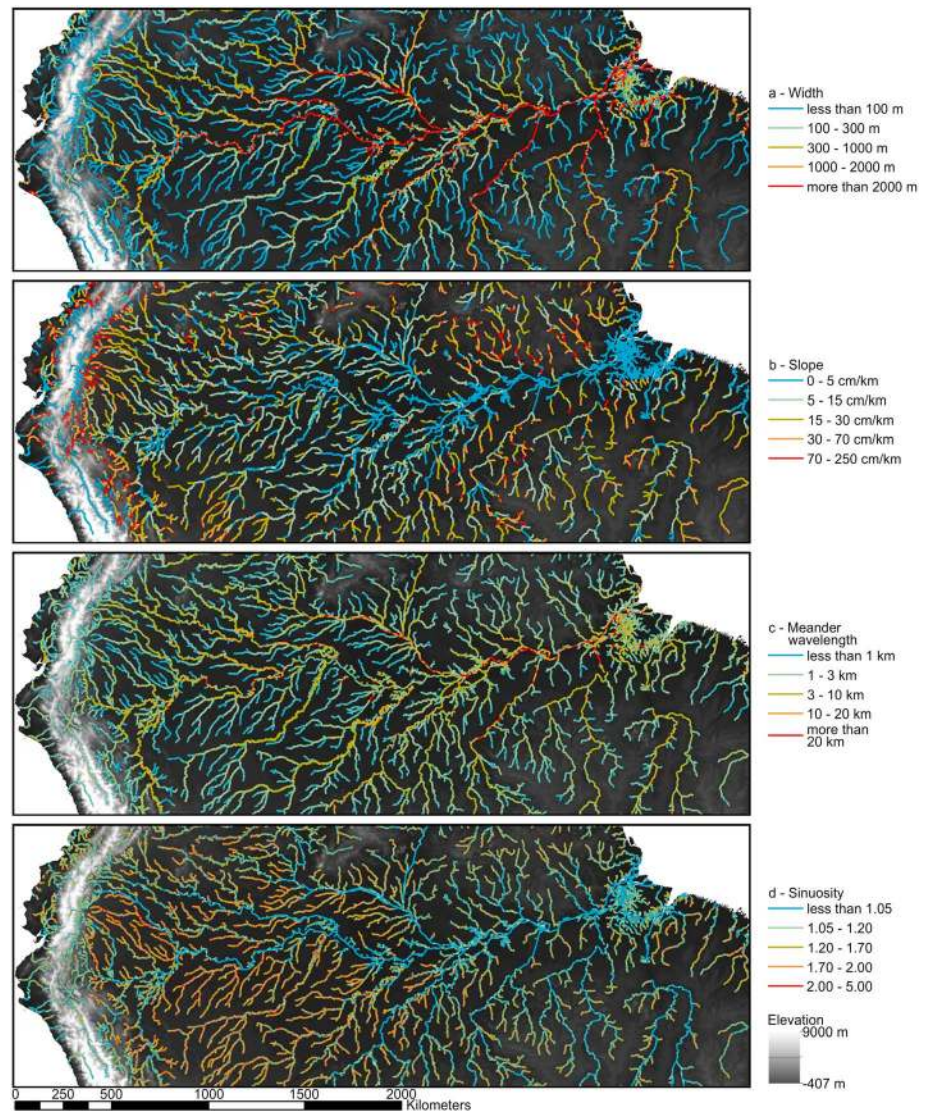


Figure 1. Evolution of the river network properties over the main stem of the Amazon River and surrounding tributaries. Panel (a) shows river width, (b) shows slopes, (c) shows river bends colored according to the meander wavelength, and (d) sinuosity. The background grayscale represents elevation according to Global 30 Arc-second elevation model.

include the computation of centerline curvature and subsequent comparison with meander wavelength and sinuosity, as well as the identification of mechanisms to explain meander scaling with respect to width based on clustering the data by river width, geographic position, soil type, and stream power for instance. Moreover, the upcoming Surface Water and Ocean Topography (SWOT) mission may offer improved water surface elevation measurements from which profile curvatures can be computed, allowing the investigation of possible relationships between river sinuosity and water surface profile curvatures as suggested by Frasson et al. (2017).

We also pursued the identification of a relationship between catchment area and width at mean annual flow. Establishing such a relationship is particularly useful for the integration of remote sensing data into hydrologic models. This integration is becoming increasingly important, especially with the anticipated 2021 launch of the first satellite specifically dedicated to hydrology, the SWOT mission. The SWOT mission uncertainties and river detection limits are often defined as functions of river width (e.g., Biancamaria et al., 2016; Domeneghetti et al., 2018; Frasson et al., 2017; Rodríguez, 2015). Nevertheless, for flood modeling or water resources management, such information is more meaningful if provided with respect to catchment area as done by Pavelsky et al. (2014). Figure 3e shows how challenging the construction of a single relationship

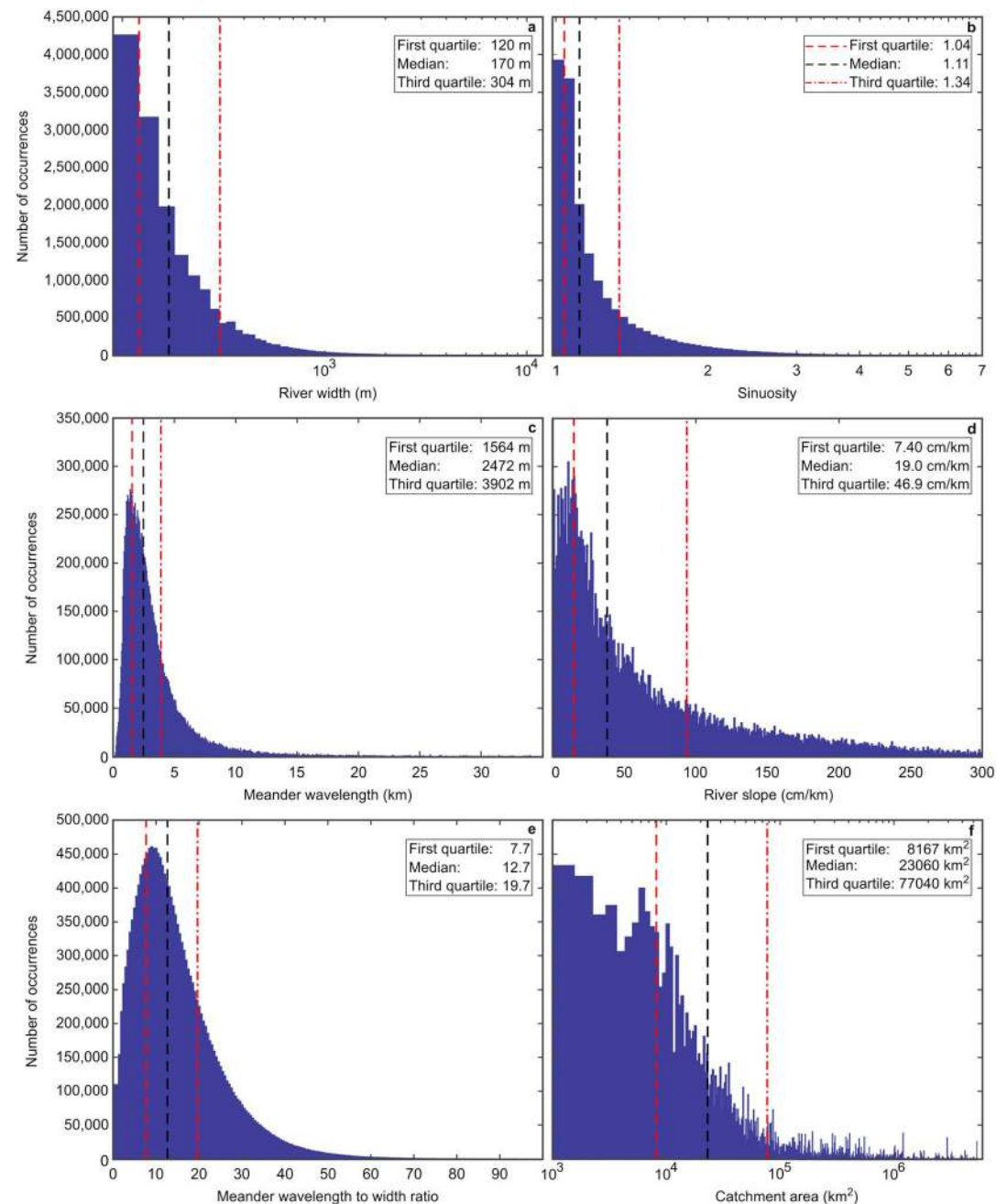


Figure 2. Histograms of global river properties. Panels show (a) width, (b) sinuosity, (c) meander wavelength, (d) water surface slope, (e) ratio between meander wavelength and width, and (f) catchment area. Only points where rivers are wider than 90 m and with sinuosity greater than 1.01 are accounted for in the histograms.

between width and catchment area at global scales can be. Such difficulty is, in part, explained by the lumping of areas with different precipitation regimes as well as limitations in estimating catchment area based on SRTM elevations and the approximations involved in the translation from number of pixels to catchment area in square kilometers. Even after applying a logarithmic transformation, the interquartile range increases considerably with increasing catchment area, indicating that heteroscedasticity is likely still present, affecting the quality of the fitted power law. Future research, including the computation of separate catchment area-width curves based on climatology, or using as a criterion the regionalization of GRDC gages (e.g., Andreadis et al., 2013) may lead to better relationships.

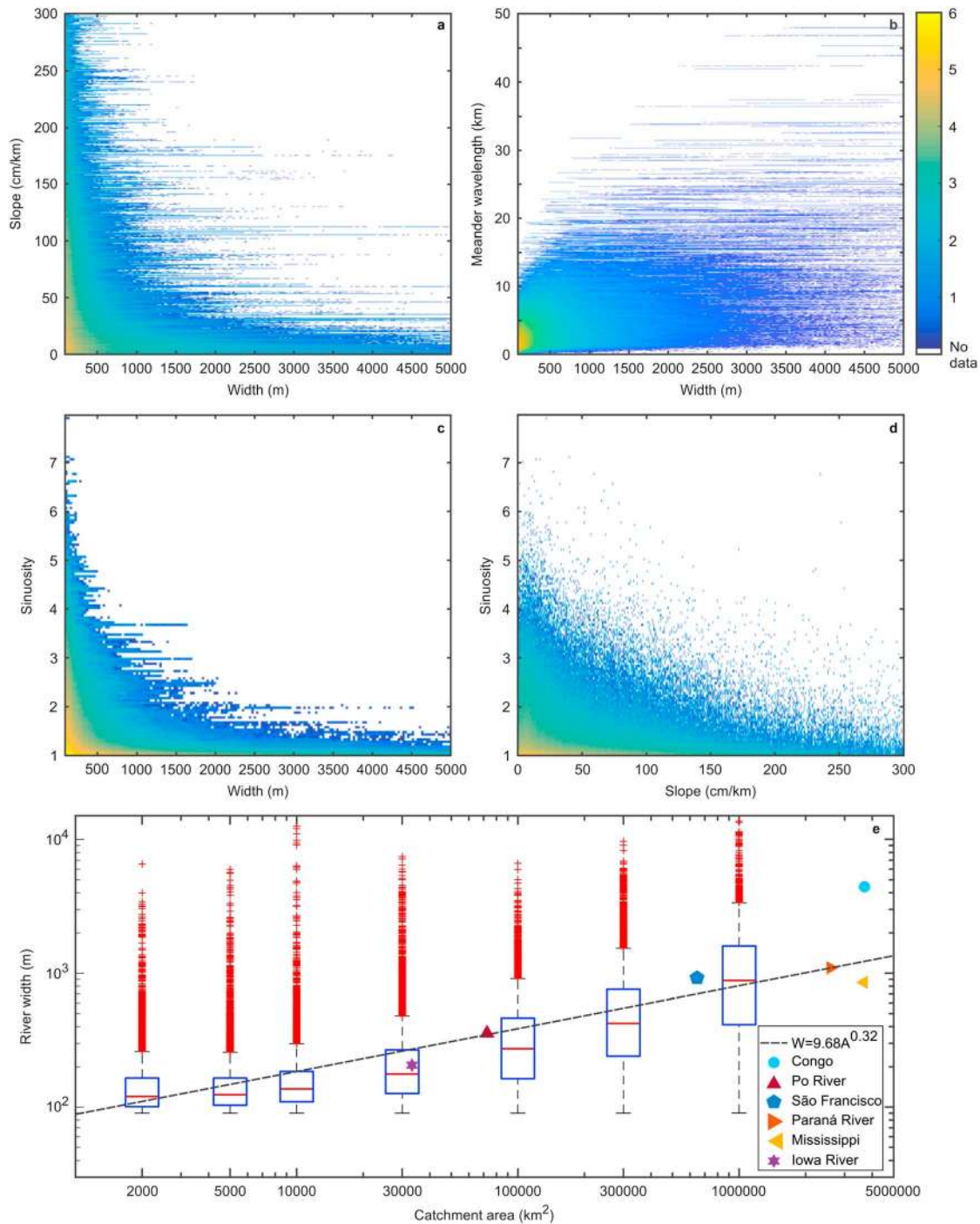


Figure 3. Global relationships between river properties. Colors represent the logarithm of the number of occurrences per bin. Panels show (a) width versus water surface slope, (b) width versus meander wavelength, (c) sinuosity versus width, (d) sinuosity versus water surface slope, (e) box plots showing the range of widths observed by catchment area bins alongside the fitted power law ($r^2 = 0.25$ computed as 1 minus the ratio between the variance of the residuals and the variance of the measured widths).

Comparing mean annual flow simulated by the water balance model WBMsed (Cohen et al., 2014) to water surface slopes (Figure 4a) leads to the same pattern as the comparison of width and slope (Figure 3a), with slope becoming shallower, on average, as both river discharge and width increase. This relationship is consistent with the expected course of rivers, running from mountains to plains, gaining volume as confluences occur, and gives us confidence in the mapping of discharge from the water balance model to our river

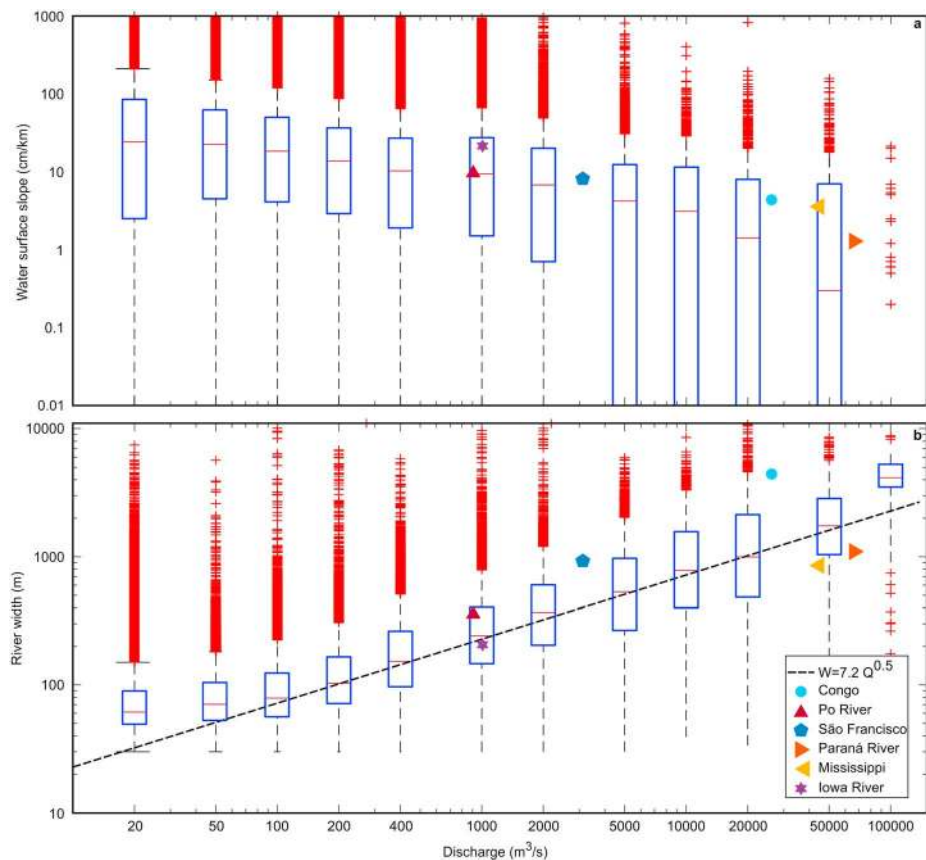


Figure 4. Relationships between modeled mean annual discharge and slope (panel (a)) and mean annual discharge and river width (b). The dashed line in the lower panel shows the power law reported by Moody and Troutman (2002).

centerlines. However, as the slopes in Figure 4a are represented in logarithm scale, the decrease in the slope standard deviation with increasing discharge is not apparent.

Additionally, incorporating the water balance model discharges into this database allows the testing of scaling laws and of relationships such as that between river width and discharge (Moody & Troutman, 2002) but with a much larger sample size. Figure 4b shows that the equation by Moody and Troutman (2002) agrees well with the medians of the discharge box plots between 100 and 5,000 m³/s. The disagreement at the lower end of the discharges may be due to the increased uncertainty in the estimation of smaller river widths, in which case our widths are likely to be over-estimated (Allen & Pavelsky, 2015). Lastly, the interquartile ranges normalized by the median width at each of the discharge classes shown in Figure 4b also provides an indication of the uncertainty associated with the discharge-width relationship derived by Moody and Troutman (2002). The normalized interquartile range varied from 85% to 165% over the discharge classes contained between 100 and 5,000 m³/s (Table S2). Although these numbers were derived based on modeled discharges and therefore should be used with caution, they provide an assessment of the predictive power of this relationship over all world rivers wider than 90 m located between 60°N and 56°S.

We opted to analyze mean annual flow for three reasons: (1) at least two of the discharge estimation algorithms expected to operate during the SWOT mission lifetime, MetroMan (Durand et al., 2014; Durand et al., 2016) and BAM (Hagemann et al., 2017), use mean annual flow to derive prior distributions for unobservable flow law parameters; (2) we aimed to keep consistency with the reported widths as those are estimated at mean annual flow; (3) mean annual flow is of interest to the study of continental scale water balances. However, the choice of mean annual flow may have prevented us from finding direct

relationships between discharge and meander wavelength and discharge sinuosity. Extension of the data set to include, for example, bankfull discharge (e.g., Bjerklie et al., 2018) or discharge with a return period of 1 to 2 years may offer further insight into meander development. Furthermore, our data set may be improved by using techniques such as hydrography-driven coarsening applied to high-resolution digital elevation models as described by Moretti and Orlandini (2018), which may lead to improved estimates of catchment areas and slopes, particularly in mountainous areas and in areas where high-resolution topographic data sets exist, for example, local LiDAR or 1 arc-second SRTM data. Additionally, exploring relationships between our center-line locations and basin and floodplain characteristics such as those cataloged by Shen et al. (2017) and Nardi et al. (2019) may lead to further insight on meander formation, flood wave propagation (e.g., Allen & Pavelsky, 2018), and refinement of local digital elevation models (Shastry & Durand, 2019).

Finally, from this data set (download instructions and metadata included in the supporting information), it is possible to compute other river properties, such as stream power normalized by width or area, opening avenues for greater insight into channel stability and, more generally, for sediment transport, especially in areas where little or no in situ information is available. Aside from these uses, further analysis and expansion of these data sets will have positive implications for upcoming remote sensing missions such as SWOT, allowing, for example, the identification of unstable planforms, where channels may migrate during the lifetime of a satellite mission and the identification of areas with similar hydraulic properties as a criterion for automated reach definition (e.g., Frasson et al., 2017).

4. Conclusion

Spatially contiguous maps of river width, slope, meander wavelength, and sinuosity fill in longstanding gaps in the knowledge of river network properties. The analysis of variations in such properties across many river networks allows identification of interconnections between planform and profile characteristics, which can now be done at continental scales. Our work presents the first look at how river width, meander wavelength, sinuosity, catchment area, slope, and discharge relate to each other on a near-global scale by combining observations of width, slope, catchment area, and modeled discharge from other existing databases with newly calculated meander wavelength and sinuosity, which were estimated, for the first time, at the global scale.

Our analysis shows strong associations between channel width and water surface slope, meander wavelength, sinuosity, and discharge. However, while width can be directly associated with the magnitude of the meander wavelength, catchment area, and discharge, it is more closely related to the range of possible values of slope and sinuosity. The direct association of width with meander wavelength and discharge is well established, but the demonstration that classical relationships hold at global scales is both novel and reassuring. More importantly, we show that there are occasions when such relationships deteriorate, indicating areas of further research. Finally, the identification of river bends and calculation of sinuosity of rivers across the globe represent a valuable first step for developing more sensible river segmentation strategies, to be applied to numerical modeling and remote sensing of rivers.

References

- Allen, G. H., Barnes, J. B., Pavelsky, T. M., & Kirby, E. (2013). Lithologic and tectonic controls on bedrock channel form at the northwest Himalayan front. *Journal of Geophysical Research: Earth Surface*, *118*, 1806–1825. <https://doi.org/10.1002/jgrf.20113>
- Allen, G. H., & Pavelsky, T. M. (2015). Patterns of river width and surface area revealed by the satellite-derived North American river width data set. *Geophysical Research Letters*, *42*, 395–402. <https://doi.org/10.1002/2014gl062764>
- Allen, G. H., & Pavelsky, T. M. (2018). Global extent of rivers and streams. *Science*, *361*, 585–588. <https://doi.org/10.1126/science.aat0636>
- Andreadis, K. M., Schumann, G. J. P., & Pavelsky, T. (2013). A simple global river bankfull width and depth database. *Water Resources Research*, *49*, 7164–7168. <https://doi.org/10.1002/wrcr.20440>
- Andreadis, K. M., Schumann, G. J. P., Stampoulis, D., Bates, P. D., Brakenridge, G. R., & Kettner, A. J. (2017). Can atmospheric reanalysis data sets be used to reproduce flooding over large scales? *Geophysical Research Letters*, *44*, 10,369–10,377. <https://doi.org/10.1002/2017GL075502>
- Biancamaria, S., Lettenmaier, D. P., & Pavelsky, T. M. (2016). The SWOT mission and its capabilities for land hydrology. *Surveys in Geophysics*, *37*(2), 307–337. <https://doi.org/10.1007/s10712-015-9346-y>
- Bjerklie, D. M. (2007). Estimating the bankfull velocity and discharge for rivers using remotely sensed river morphology information. *Journal of Hydrology*, *341*(3–4), 144–155. <https://doi.org/10.1016/j.jhydrol.2007.04.011>
- Bjerklie, D. M., Birkett, C. M., Jones, J. W., Carabajal, C., Rover, J. A., Fulton, J. W., & Garambois, P.-A. (2018). Satellite remote sensing estimation of river discharge: Application to the Yukon River Alaska. *Journal of Hydrology*, *561*, 1000–1018. <https://doi.org/10.1016/j.jhydrol.2018.04.005>

Acknowledgments

We would like to acknowledge the financial support received through the NASA SWOT Science Team funding (NNX16AH82G) and the SWOT Algorithm Definition Team (ADT) contract to the Ohio State University and the University of North Carolina. G. Schumann's time was also supported by a SWOT ADT contract. We also thank Mark Hagemann for his assistance with fitting the power law to the width-catchment area data set and the computation of the fit statistics. The Water Balance Model data used in this study were provided by Albert Kettner from the INSTAAR, University of Colorado at Boulder. GTOPO 30 data were distributed by the Land Processes Distributed Active Archive Center (LP DAAC), located at USGS/EROS, Sioux Falls, SD. The data set produced in this study are openly available from Frasson et al. (2019) under a Creative Commons Attribution License in shapefile format. A more complete version with 30 m posting is available in the netcdf format upon request. Metadata describing the data set can be found in the supporting information. Finally, we would like to thank the insightful and constructive comments provided by two anonymous reviewers and the editor.

- Bjerklie, D. M., Moller, D., Smith, L. C., & Dingman, S. L. (2005). Estimating discharge in rivers using remotely sensed hydraulic information. *Journal of Hydrology*, 309(1–4), 191–209. <https://doi.org/10.1016/j.jhydrol.2004.11.022>
- Brakenridge, G. R. (2018). Flood risk mapping from orbital remote sensing. In G. J.-P. Schumann, P. D. Bates, A. Heiko, & G. T. Aronica (Eds.), *Global flood hazard: Applications in modeling, mapping, and forecasting* (pp. 43–54). Hoboken, NJ: American Geophysical Union and John Wiley & Sons, Inc. <https://doi.org/10.1002/9781119217886.ch3>
- Brakenridge, G. R., Nghiem, S. V., Anderson, E., & Mic, R. (2007). Orbital microwave measurement of river discharge and ice status. *Water Resources Research*, 43, W04404. <https://doi.org/10.1029/2006WR005238>
- Cohen, S., Kettner, A. J., & Syvitski, J. P. M. (2014). Global suspended sediment and water discharge dynamics between 1960 and 2010: Continental trends and intra-basin sensitivity. *Global and Planetary Change*, 115, 44–58. <https://doi.org/10.1016/j.gloplacha.2014.01.011>
- Constantine, J. A., Dunne, T., Ahmed, J., Legleiter, C., & Lazarus, E. D. (2014). Sediment supply as a driver of river meandering and floodplain evolution in the Amazon basin. *Nature Geoscience*, 7, 899–903. <https://doi.org/10.1038/ngeo2282>, <https://www.nature.com/articles/ngeo2282#supplementary-information>
- Domeneghetti, A., Schumann, G. J. P., Frasson, R. P. M., Wei, R., Pavelsky, T. M., Castellarin, A., et al. (2018). Characterizing water surface elevation under different flow conditions for the upcoming SWOT mission. *Journal of Hydrology*, 561, 848–861. <https://doi.org/10.1016/j.jhydrol.2018.04.046>
- Durand, M., Gleason, C. J., Garambois, P. A., Bjerklie, D., Smith, L. C., Roux, H., et al. (2016). An intercomparison of remote sensing river discharge estimation algorithms from measurements of river height, width, and slope. *Water Resources Research*, 52, 4527–4549. <https://doi.org/10.1002/2015wr018434>
- Durand, M., Neal, J., Rodríguez, E., Andreadis, K. M., Smith, L. C., & Yoon, Y. (2014). Estimating reach-averaged discharge for the River Severn from measurements of river water surface elevation and slope. *Journal of Hydrology*, 511, 92–104. <https://doi.org/10.1016/j.jhydrol.2013.12.050>
- Edwards, B. F., & Smith, D. H. (2002). River meandering dynamics. *Physical Review E*, 65(4), 046303. <https://doi.org/10.1103/PhysRevE.65.046303>
- Farr, T. G., Rosen, P. A., Caro, E., Crippen, R., Duren, R., Hensley, S., et al. (2007). The shuttle radar topography mission. *Reviews of Geophysics*, 45, RG2004. <https://doi.org/10.1029/2005RG000183>
- Frasson, R. P. d. M., T. M. Pavelsky, M. A. Fonstad, M. T. Durand, G. H. Allen, G. Schumann, et al. (2019). Global database of river width, slope, catchment area, meander wavelength, sinuosity, and discharge. Zenodo. <https://doi.org/10.5281/zenodo.2579160>
- Frasson, R. P. d. M., Wei, R., Durand, M., Minear, J. T., Domeneghetti, A., Schumann, G., et al. (2017). Automated river reach definition strategies: Applications for the surface water and ocean topography mission. *Water Resources Research*, 53, 8164–8186. <https://doi.org/10.1002/2017wr020887>
- Gleason, C. J., & Smith, L. C. (2014). Toward global mapping of river discharge using satellite images and at-many-stations hydraulic geometry. *Proceedings of the National Academy of Sciences of the United States of America*, 111(13), 4788–4791. <https://doi.org/10.1073/pnas.1317606111>
- Gleason, C. J., Smith, L. C., & Lee, J. (2014). Retrieval of river discharge solely from satellite imagery and at-many-stations hydraulic geometry: Sensitivity to river form and optimization parameters. *Water Resources Research*, 50, 9604–9619. <https://doi.org/10.1002/2014wr016109>
- Gleason, C. J., & Wang, J. (2015). Theoretical basis for at-many-stations hydraulic geometry. *Geophysical Research Letters*, 42, 7107–7114. <https://doi.org/10.1002/2015GL064935>
- GRDC (2011). In G. R. D. Centre (Ed.), *Long-term mean monthly discharges and annual characteristics of GRDC station*. Koblenz, Germany: Federal Institute of Hydrology (BfG).
- Hagemann, M. W., Gleason, C. J., & Durand, M. T. (2017). Bam: Bayesian AMHG-Manning inference of discharge using remotely sensed stream width, slope, and height. *Water Resources Research*, 53, 9692–9707. <https://doi.org/10.1002/2017WR021626>
- Kiel, B. A. (2015). Measurements of US rivers clarify river-shaping factors and interactions with groundwater, (Doctoral dissertation). Retrieved from UT Electronic Theses and Dissertations. Austin, TX: the University of Texas at Austin. <https://repositories.lib.utexas.edu/handle/2152/32617>
- LeFavour, G., & Alsdorf, D. (2005). Water slope and discharge in the Amazon River estimated using the shuttle radar topography mission digital elevation model. *Geophysical Research Letters*, 32, L17404. <https://doi.org/10.1029/2005GL023836>
- Lehner, B., & Grill, G. (2013). Global river hydrography and network routing: Baseline data and new approaches to study the world's large river systems. *Hydrological Processes*, 27(15), 2171–2186. <https://doi.org/10.1002/hyp.9740>
- Lehner, B., Verdin, K., & Jarvis, A. (2008). New global hydrography derived from spaceborne elevation data. *Eos, Transactions American Geophysical Union*, 89(10), 93–94. <https://doi.org/10.1029/2008EO100001>
- Leopold, L. B., & Wolman, M. G. (1957). *River channel patterns: Braided, meandering, and straight*, US Government Printing Office. Washington, DC.
- Leopold, L. B., & Wolman, M. G. (1960). River meanders. *Geological Society of America Bulletin*, 71(6), 769–793. [https://doi.org/10.1130/0016-7606\(1960\)71\[769:RM\]2.0.CO;2](https://doi.org/10.1130/0016-7606(1960)71[769:RM]2.0.CO;2)
- Li, J., & Sheng, Y. (2012). An automated scheme for glacial lake dynamics mapping using Landsat imagery and digital elevation models: A case study in the Himalayas. *International Journal of Remote Sensing*, 33(16), 5194–5213. <https://doi.org/10.1080/01431161.2012.657370>
- Manuilova, E., Schuetzenmeister, A., & Model, F. (2014). Method comparison regression, R package version 1.2.1.
- Marcus, W. A., & Fonstad, M. A. (2008). Optical remote mapping of rivers at sub-meter resolutions and watershed extents. *Earth Surface Processes and Landforms*, 33(1), 4–24. <https://doi.org/10.1002/esp.1637>
- Mark, D. M., & Church, M. G. (1977). On the misuse of regression in. *Earth Science*, 9(1), 63–75. <https://doi.org/10.1007/bf02312496>
- Moody, J. A., & Troutman, B. M. (2002). Characterization of the spatial variability of channel morphology. *Earth Surface Processes and Landforms*, 27(12), 1251–1266. <https://doi.org/10.1002/esp.403>
- Moretti, G., & Orlandini, S. (2018). Hydrography-driven coarsening of grid digital elevation models. *Water Resources Research*, 54, 3654–3672. <https://doi.org/10.1029/2017WR021206>
- Nardi, F., Annis, A., Di Baldassarre, G., Vivoni, E. R., & Grimaldi, S. (2019). GFPLAIN250m, a global high-resolution dataset of Earth's floodplains. *Scientific Data*, 6, 180309. <https://doi.org/10.1038/sdata.2018.309>
- Pavelsky, T. M., Durand, M. T., Andreadis, K. M., Beighley, R. E., Paiva, R. C. D., Allen, G. H., & Miller, Z. F. (2014). Assessing the potential global extent of SWOT river discharge observations. *Journal of Hydrology*, 519, 1516–1525. <https://doi.org/10.1016/j.jhydrol.2014.08.044>
- Pavelsky, T. M., & Smith, L. C. (2008). RivWidth: A software tool for the calculation of river widths from remotely sensed imagery. *IEEE Geoscience and Remote Sensing Letters*, 5(1), 70–73. <https://doi.org/10.1109/lgrs.2007.908305>

- Richards, K. S. (1976). The morphology of riffle-pool sequences. *Earth Surface Processes and Landforms*, *1*(1), 71–88. <https://doi.org/10.1002/esp.3290010108>
- Richards, K. S. (1982). *Rivers: Form and process in alluvial channels*. Methuen, London; New York.
- Rodríguez, E. (2015). Surface water and ocean topography mission (SWOT), science requirements document Rep. JPL document D-61923 Jet Propulsion Laboratory. Retrieved from https://swot.jpl.nasa.gov/files/swot/SRD_021215.pdf
- Seminara, G. (2006). Meanders. *Journal of Fluid Mechanics*, *554*, 271–297. <https://doi.org/10.1017/S0022112006008925>
- Sen, P. K. (1968). Estimates of the regression coefficient based on Kendall's tau. *Journal of the American Statistical Association*, *63*(324), 1379–1389. <https://doi.org/10.1080/01621459.1968.10480934>
- Shastry, A., & Durand, M. (2019). Utilizing flood inundation observations to obtain floodplain topography in data-scarce regions. *Frontiers in Earth Science*, *6*. <https://doi.org/10.3389/feart.2018.00243>
- Shen, X., Anagnostou, E. N., Mei, Y., & Hong, Y. (2017). A global distributed basin morphometric dataset. *Scientific Data*, *4*, 160124. <https://doi.org/10.1038/sdata.2016.124>
- Tarpanelli, A., Barbetta, S., Brocca, L., & Moramarco, T. (2013). River discharge estimation by using altimetry data and simplified flood routing modeling. *Remote Sensing*, *5*(9), 4145. <http://www.mdpi.com/2072-4292/5/9/4145>
- Theil, H. (1992). A rank-invariant method of linear and polynomial regression analysis. In B. Raj & J. Koerts (Eds.), *Henri Theil's contributions to economics and econometrics. Advanced studies in theoretical and applied econometrics* (pp. 1397–1412). Dordrecht: Springer. https://doi.org/10.1007/978-94-011-2546-8_20
- Tourian, M. J., Schwatke, C., & Sneeuw, N. (2017). River discharge estimation at daily resolution from satellite altimetry over an entire river basin. *Journal of Hydrology*, *546*, 230–247. <https://doi.org/10.1016/j.jhydrol.2017.01.009>
- Tourian, M. J., Sneeuw, N., & Bárdossy, A. (2013). A quantile function approach to discharge estimation from satellite altimetry (ENVISAT). *Water Resources Research*, *49*, 4174–4186. <https://doi.org/10.1002/wrcr.20348>
- Van Dijk, A. I. J. M., Brakenridge, G. R., Kettner, A. J., Beck, H. E., De Groeve, T., & Schellekens, J. (2016). River gauging at global scale using optical and passive microwave remote sensing. *Water Resources Research*, *52*, 6404–6418. <https://doi.org/10.1002/2015wr018545>
- Williams, G. P. (1986). River meanders and channel size. *Journal of Hydrology*, *88*(1-2), 147–164. [https://doi.org/10.1016/0022-1694\(86\)90202-7](https://doi.org/10.1016/0022-1694(86)90202-7)
- Xu, H. (2006). Modification of normalised difference water index (NDWI) to enhance open water features in remotely sensed imagery. *International Journal of Remote Sensing*, *27*(14), 3025–3033. <https://doi.org/10.1080/01431160600589179>
- Yamazaki, D., O'Loughlin, F., Trigg, M. A., Miller, Z. F., Pavelsky, T. M., & Bates, P. D. (2014). Development of the global width database for large rivers. *Water Resources Research*, *50*, 3467–3480. <https://doi.org/10.1002/2013WR014664>
- Zobler, L. (1999). Global soil types, 1-degree grid (Zobler). Oak Ridge National Laboratory Distributed Active Archive Center. <https://doi.org/10.3334/ORNLDAAAC/418>